


Article

# Hydrous Molybdenum Oxide Coating of Zinc Metal Anode via the Facile Electrodeposition Strategy and Its Performance Improvement Mechanisms for Aqueous Zinc–Ion Batteries

Jianwei Yuan , Yutao Shi, Weibai Bian, Huaren Wu, Yingjun Chen, Chengcheng Zhou, Xiaohui Chen \*, Wei Zhang and Hailin Shen \*

School of Chemical Engineering and Materials, Changzhou Institute of Technology, Changzhou 213022, China; yuanjw@czust.edu.cn (J.Y.)

\* Correspondence: chenxh@czust.edu.cn (X.C.); shenhailin@czust.edu.cn (H.S.)

**Abstract:** Aqueous zinc–ion batteries (ZIBs) are widely recognized as highly promising energy storage devices because of their inherent characteristics, including superior safety, affordability, eco–friendliness, and various other benefits. However, the significant corrosion of the zinc metal anode, side reactions occurring between the anode and electrolyte, and the formation of zinc dendrites significantly hinder the practical utilization of ZIBs. Herein, we utilized an electrodeposition method to apply a unique hydrous molybdenum oxide (HMoO<sub>x</sub>) layer onto the surface of the zinc metal anode, aiming to mitigate its corrosion and side reactions during the process of zinc deposition and stripping. In addition, the HMoO<sub>x</sub> layer not only improved the hydrophilicity of the zinc anode, but also adjusted the migration of Zn<sup>2+</sup>, thus facilitating the uniform deposition of Zn<sup>2+</sup> to reduce dendrite formation. A symmetrical cell with the HMoO<sub>x</sub>–Zn anode displayed reduced–voltage hysteresis (80 mV at 2.5 mA/cm<sup>2</sup>) and outstanding cycle stability after 3000 cycles, surpassing the performance of the uncoated Zn anode. Moreover, the HMoO<sub>x</sub>–Zn anode coupled with a γ–MnO<sub>2</sub> cathode created a considerably more stable rechargeable full battery compared to the bare Zn anode. The HMoO<sub>x</sub>–Zn || γ–MnO<sub>2</sub> full cell also displayed excellent cycling stability with a charge/discharge–specific capacity of 129/133 mAh g<sup>–1</sup> after 300 cycles. In summary, this research offers a straightforward and advantageous approach that can significantly contribute to the future advancements in rechargeable ZIBs.

**Keywords:** electrodeposition; anode; HMoO<sub>x</sub> coating; protection; aqueous zinc–ion battery



**Citation:** Yuan, J.; Shi, Y.; Bian, W.; Wu, H.; Chen, Y.; Zhou, C.; Chen, X.; Zhang, W.; Shen, H. Hydrous Molybdenum Oxide Coating of Zinc Metal Anode via the Facile Electrodeposition Strategy and Its Performance Improvement Mechanisms for Aqueous Zinc–Ion Batteries. *Molecules* **2024**, *29*, 3229. <https://doi.org/10.3390/molecules29133229>

Academic Editor: Gregorio F. Ortiz

Received: 8 June 2024

Revised: 27 June 2024

Accepted: 5 July 2024

Published: 8 July 2024



**Copyright:** © 2024 by the authors. Licensee MDPI, Basel, Switzerland. This article is an open access article distributed under the terms and conditions of the Creative Commons Attribution (CC BY) license (<https://creativecommons.org/licenses/by/4.0/>).

## 1. Introduction

As coal and other fossil fuel resources have been excessively depleted, a plethora of new rechargeable batteries have emerged, including lithium–ion batteries (LIBs) [1], zinc–ion batteries (ZIBs) [2], magnesium–ion batteries [3], sodium–ion batteries [4], and aluminum–ion batteries [5–7], revolutionizing the way we power portable electronic devices and vehicles. Among the emerging battery technologies, aqueous ZIBs are particularly favored for the extensive energy storage applications owing to their notable features, including enhanced safety, affordability, lack of pollution, convenient assembly, and high specific/volumetric capacity [8–12].

Conventional ZIBs are assembled by the cathode (MnO<sub>2</sub>) and anode (Zn metal), which show poor cycling stability. The performance of ZIBs heavily relies on the zinc anode, which faces numerous challenges. Side reactions, such as corrosion and the hydrogen evolution reaction (HER) during the charging and discharging processes, are a key factor affecting the performance of the Zn anode. Zn is prone to corrosion when exposed to the electrolyte, resulting in the formation of zinc oxide or hydroxide, and HER leads to the loss of active material and decreased battery efficiency [13–15]. More importantly, the uncontrolled growth of dendrites can occur during the charging/discharging processes, which are

needle-like structures that can penetrate the separator and result in short circuits, thus posing safety risks. Hence, for the successful commercialization of ZIBs, it is imperative to explore effective strategies to protect the zinc anode by controlling the side reactions and dendrite growth. To date, numerous effective strategies have been suggested to tackle the aforementioned concerns, including zinc alloying [16], three-dimensional structure design [17,18], surface modification [19,20], electrolyte modification [21–23], separator design [24], etc. Among them, surface coating is considered a simple and effective strategy. The coating materials for modifying the Zn anode include carbons (e.g., graphene oxide [25], carbon black [26], and carbon nanotubes [27]), metal compounds (e.g., ZnS [28], Al<sub>2</sub>O<sub>3</sub> [29], CaCO<sub>3</sub> [19], and ZrO<sub>2</sub> [30]), organic polymers (e.g.,  $\beta$ -phase poly(vinylidene difluoride) ( $\beta$ -PVDF) [31], polyamide ((PA)@Zn(TfO)<sub>2</sub>) [32], polypyrrole (PPy) [33]), MOFs (zeolitic imidazolate framework-8 (ZIF-8) [34], zeolitic imidazolate framework-7 (ZIF-7) [35], and Universitetet/Oslo-66 (UIO-66) MOFs [36]). The inorganic coatings are more effective at restraining dendrite growth because of their physical characteristics, such as high mechanical strength and rigidity, whereas the polymer coating is susceptible to puncture by dendrites due to its flexibility [37].

Previously, Liu et al. proposed an amorphous MoO<sub>x</sub> electrode as the anode material for aqueous NH<sub>4</sub><sup>+</sup>-ion batteries, which displayed high gravimetric/areal capacities of 175 mAh g<sup>-1</sup> at 0.22 A g<sup>-1</sup>. The spectroscopic investigations carried out to understand the charge storage mechanism of MoO<sub>x</sub> indicate that the MnO<sub>x</sub> anode facilitates the rapid transportation of NH<sub>4</sub><sup>+</sup> via hydrogen bond formation and breaking [38]. In addition, a few examples (e.g., MoO<sub>2</sub>/carbon [39] and MoO<sub>3-x</sub>/Mxene [40]) have been recently employed to investigate Zn<sup>2+</sup> storage behavior because of their inherent multiple valence states, along with significant theoretical capacity, electron-conducting ability, and robust structural stability. Molybdenum oxides, as a stable oxide and electrode material, can provide a more stable interface, but can also improve electron and ion transport, and improve reaction kinetics; hence, molybdenum oxides can be used as a protective layer of a Zn negative electrode. The electrochemical properties of the Zn anode modified by a molybdenum oxide layer are far from what were expected. In contrast to the hydrophobic layer, the hydrophilic layer can be selective when modifying the transport characteristics of Zn<sup>2+</sup>, thus improving the transport efficiency of zinc ions. The hydrophilic surface can also improve the contact between the electrolyte and the electrode, helping Zn<sup>2+</sup> to deposit more evenly on the anode's surface. In addition, the hydrophilic layer helps to reduce electrolyte decomposition, hydrogen release, and other side reactions. For example, Li et al. discovered that a TiO<sub>2</sub>-coated Zn anode exhibited improved surface wettability compared to the uncoated Zn. This enhancement facilitated the movement and even the deposition of Zn<sup>2+</sup>, while also reducing the charge transfer resistance [41]. Therefore, the HMoO<sub>x</sub> layer combines the advantages of molybdenum oxide and the hydrophilic surface, which can effectively inhibit the corrosion, side reactions, and zinc dendrite growth during zinc deposition/stripping. To our knowledge, there are no relevant studies on HMoO<sub>x</sub> as a protective coating applied onto the surface of zinc at present.

There are various methods to establish a protective layer on the zinc anode's surface, primarily focusing on physical coating and in situ synthesis. Unlike them, the electrodeposition method is a relatively simple and easy-to-operate technique. The thickness, uniformity, and consistency of a protective film can be precisely controlled by adjusting the deposition parameters, which can enhance the performance consistency of the battery. Noori et al. reported that the electrodeposition method can produce the thinnest and most uniform few-layer, thin MoS<sub>2</sub> films on a graphene electrode [42]. Bhojate et al. employed an electrochemical deposition method to produce a distinctive 2D MoS<sub>2</sub> layer on a zinc anode [43]. Cao et al. have successfully electrochemically deposited MoO<sub>2</sub> from an ammonium molybdate solution and systematically explored how variations in electrolyte composition and deposition conditions impact the characteristics of MoO<sub>2</sub> [44].

Herein, we present a rapid and straightforward method for coating the surface of the Zn anode with HMoO<sub>x</sub> via constant potential deposition. By optimizing the deposition

time, the final oxidation layer with the best performance is obtained, and the film thickness can be finely adjusted on the nanometer scale. This demonstrates a significant improvement compared with the bare Zn, and the results show that based on the metal surface forming a thin zinc molybdenum oxide hydrate layer, there is an even distribution of the lead zinc metal surface electric field. The  $\text{HMoO}_x$  coating aids in enhancing the migration of  $\text{Zn}^{2+}$  ions, ensuring uniform deposition, and consequently enhancing the overall performance of the battery. The  $\text{HMoO}_x$ -coated Zn foil (denoted as  $\text{HMoO}_x$ -Zn) was utilized to assemble the symmetric cells, which can display a more stable cycle stability and reduced-voltage hysteresis of  $\sim 103$  mV than the bare Zn anode at  $2.5 \text{ mA cm}^{-2}$ . Simultaneously, the  $\text{HMoO}_x$ -Zn ||  $\gamma$ - $\text{MnO}_2$  full cell also exhibited exceptional stability over numerous cycles, maintaining a charge/discharge-specific capacity of 129/133.1  $\text{mAh g}^{-1}$  after 300 cycles. This work, therefore, offers valuable insights into the development of a highly reversible Zn anode.

## 2. Results and Discussion

The  $\text{HMoO}_x$ -Zn anode was prepared throughout this project using a simple constant-potential electro-deposition method, as shown in Figure 1a. At  $-0.8$  V vs. SCE, the  $(\text{NH}_4)_2\text{MoS}_4$  solution with a concentration of 5 mM began to undergo reduction on the surface of Zn, forming  $\text{MoO}_4^{2-}$  ions [44]. As shown in Figure 1b, the deposition time of the reduction process was altered to adjust the thickness of the  $\text{HMoO}_x$  layer, and the  $\text{HMoO}_x$ -Zn anode surface presented a distinct color compared to the bare zinc. With the increase in the deposition time, the surface color of the  $\text{HMoO}_x$ -Zn anode deepened, which is consistent with the theoretical inference that the  $\text{HMoO}_x$  coating is thicker with a longer deposition time.

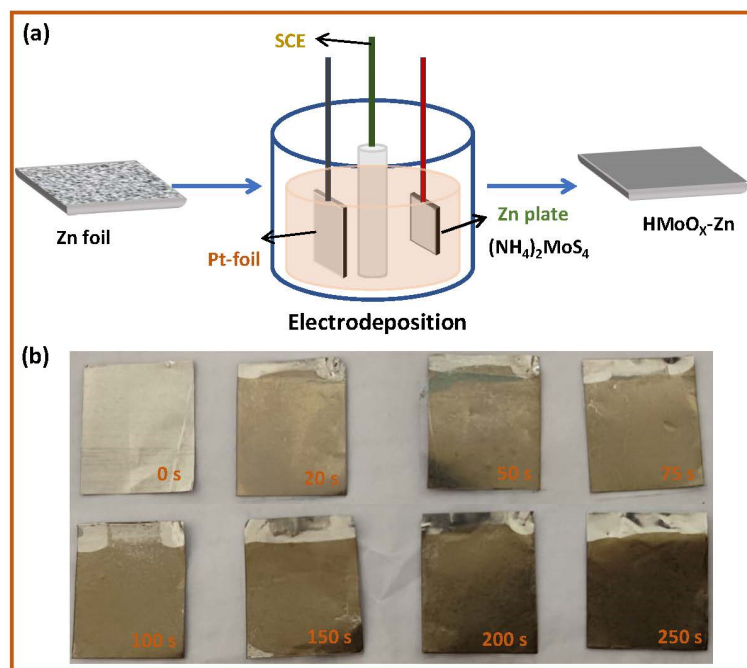


**Figure 1.** The preparation of the  $\text{HMoO}_x$ -Zn anode. (a) The synthesis process of the  $\text{HMoO}_x$ -Zn anode via electrodeposition. (b) The digital pictures of the  $\text{HMoO}_x$ -Zn anode at different deposition times (0 s, 20 s, 50 s, 75 s, 100 s, 150 s, 200 s, and 250 s).

The effect of electrodeposition varied with changes in the duration of the reduction process's deposition, as illustrated in Figures 2a–d and S1. The SEM images illustrated that the increase in the electrodeposition time resulted in an increase in the incidence of cracking in the  $\text{HMoO}_x$  layer. The electrodeposition time of 75 s was considered as an optimum time for a uniform  $\text{HMoO}_x$  coating on the Zn surface, while at 250 s, the  $\text{HMoO}_x$

layer demonstrated non-uniform fragments and higher surface resistance. Galvanostatic charge/discharge measurements were conducted on symmetrical batteries to evaluate the effect of the ammonium molybdate electrodeposition time on the electrochemical properties of  $\text{HMoO}_x\text{-Zn}$  anodes in Figures 2e and S2. The  $\text{HMoO}_x\text{-Zn}$  anode showed excellent cycle stability when the deposition time reached 20 s; however, its stripping/deposition voltage range was wide. With the increase in the electrochemical deposition time, the charge-discharge voltage range narrowed until the deposition time was 75 s, and the voltage difference was at its narrowest. However, the stability of the  $\text{HMoO}_x\text{-Zn}$  anode diminished with the prolonged deposition time. The performance results align with the SEM analysis described earlier. Therefore, the electrodeposition time of 75 s was considered the optimal duration for uniformly applying the  $\text{HMoO}_x$  coating on the Zn surface.

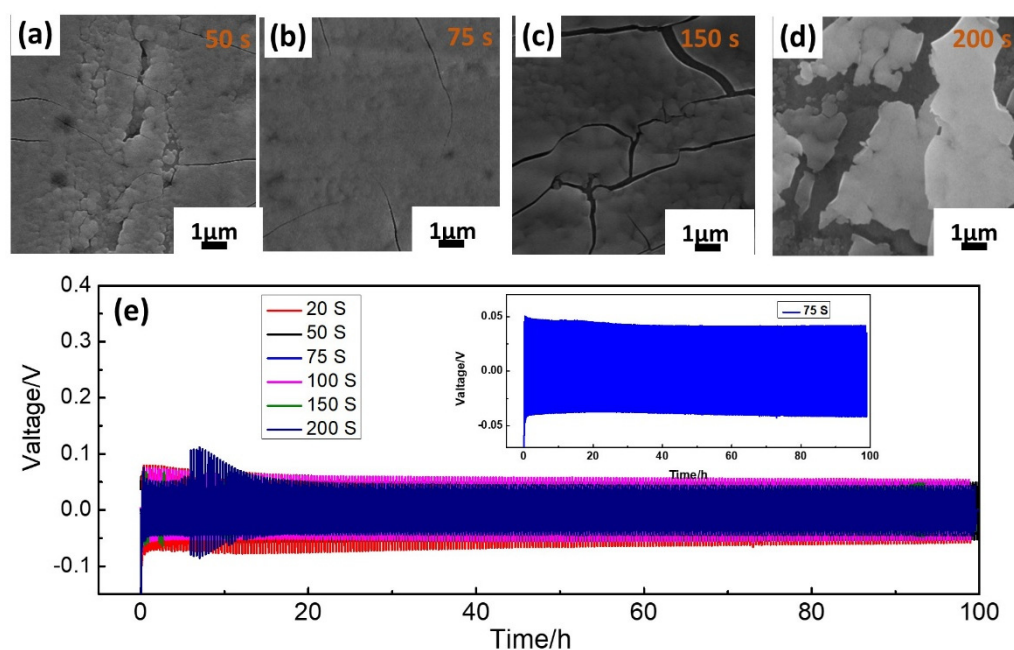


**Figure 2.** The optimization of preparation of the  $\text{HMoO}_x\text{-Zn}$  anode. (a–d) The SEM of the  $\text{HMoO}_x\text{-Zn}$  anode at different deposition times of 50 s, 75 s, 150 s, and 250 s, respectively. (e) The dynamic measurements of a symmetric cell for  $\text{HMoO}_x\text{-Zn}$  anodes for 20 s, 50 s, 75 s, 100 s, 150 s, and 200 s in stripping/plating cycles (300 cycles, 2.5 mA cm<sup>-2</sup>), respectively. The illustration in Figure 2e shows magnified information corresponding to 75 s. The stripping/plating time of anodes was 10 min for each cycle.

To analyze the surface elemental composition of  $\text{HMoO}_x\text{-Zn}$ , XPS was utilized to measure the sample. As depicted in Figure 3a, the displayed spectrum peaks were attributed to the elements depicted, including Zn, O, Mo, and C. The peaks associated with  $\text{Zn}2p_{3/2}$  and  $\text{Zn}2p_{1/2}$  were observed at 1021.69 eV and 1046.03 eV, respectively [45]. The splitting of Mo 3d peaks were detected at 232.2 eV for  $\text{Mo}^{6+} 3d_{5/2}$ , 235.1 eV for  $\text{Mo}^{6+} 3d_{3/2}$ , 231.1 eV for  $\text{Mo}^{4+} 3d_{5/2}$ , and 234.4 eV for  $\text{Mo}^{4+} 3d_{3/2}$  in Figure 3b [46]. Additionally, the O 1s peaks at 530.6 eV, 532.2 eV, and 533.4 eV for  $\text{HMoO}_x\text{-Zn}$  were fitted, attributed to Mo–O–Mo, Mo–O–H, and H–O–H in Figure 3c, respectively [46,47]. In addition, the top-view SEM images provided insight into the morphological attributes of the bare Zn in Figure 3d and  $\text{HMoO}_x\text{-Zn}$  in Figure 3e. The bare Zn exhibited an uneven surface with a particulate structure, potentially amplifying dendrite formation, thus further intensifying the decline in cyclic performance. As shown in Figures 3f and S3, there was a uniform and smooth layer of  $\text{HMoO}_x$  on the surface of the  $\text{HMoO}_x\text{-Zn}$  foil. It was reported that the protective layer can enhance the stability of the anode interface and promote the formation of a stable electrolyte/electrode interface [41].



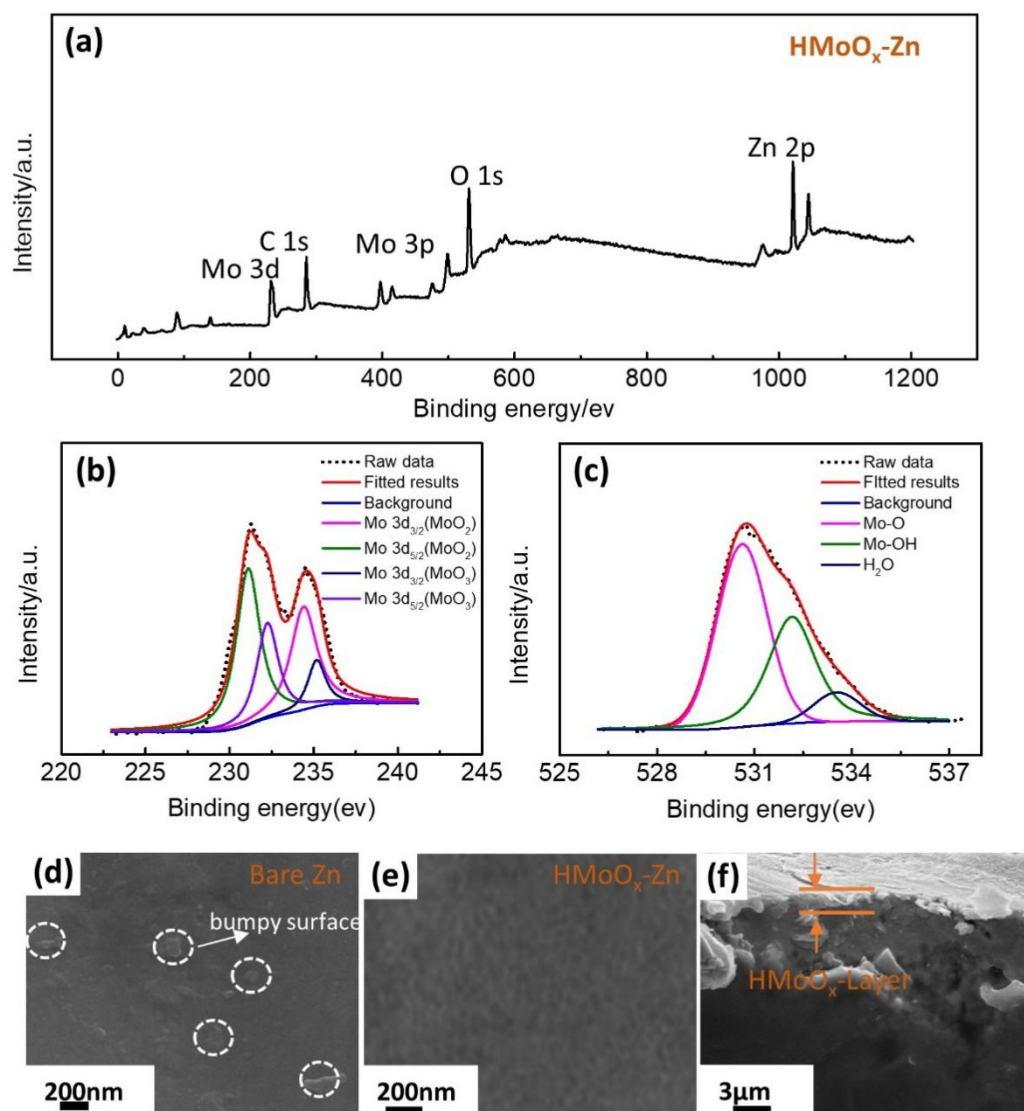


**Figure 3.** The composition and morphology of analysis for  $\text{HMoO}_x\text{-Zn}$ . (a) The XPS survey spectrum of  $\text{HMoO}_x\text{-Zn}$ . The high-resolution XPS spectroscopy measurements of the Mo 2p (b) and O 1s (c). The SEM images of bare Zn (d) and  $\text{HMoO}_x\text{-Zn}$  (e). (f) The cross-sectional SEM image of the  $\text{HMoO}_x\text{-Zn}$ .

The electrochemical plating/stripping characteristics of zinc were examined using symmetric  $\text{Zn}||\text{Zn}$  and  $\text{HMoO}_x\text{-Zn}||\text{HMoO}_x\text{-Zn}$  half cells, as shown in Figure 4a. The bare Zn electrodes (230 mV) showed a significantly higher overpotential than the  $\text{HMoO}_x\text{-Zn}$  anodes (150 mV). In addition, the bare Zn-based symmetric cells experienced failure after several limited cycles due to noticeable voltage fluctuations and irregular voltage hysteresis. Conversely, the  $\text{HMoO}_x$ -coated anodes demonstrated remarkable endurance, maintaining an exceptionally low-voltage hysteresis of 80 mV at  $2.5 \text{ mA cm}^{-2}$  for over 3000 cycles. The overpotential of the  $\text{HMoO}_x\text{-Zn}$  anodes (220 mV) was also lower compared to that of the bare Zn (103 mV) at the 16th cycle. This suggested that the introduction of the  $\text{HMoO}_x$  coating could effectively suppress dendrite formation and mitigate side reactions taking place at the interface between the electrode and electrolyte [19,29]. Moreover, conducting continuous galvanostatic charge/discharge over a range of current densities from 0.25 to  $5 \text{ mA cm}^{-2}$  was employed to assess the rate capability of the two electrodes, as shown in Figure 4b. With increasing current density, the  $\text{HMoO}_x\text{-Zn}$  anodes exhibited a stable voltage plateau and minimal voltage hysteresis, which could be attributed to the protective  $\text{HMoO}_x$  layer. In contrast, bare Zn electrodes demonstrated an erratic

voltage distribution and significant voltage hysteresis.  $\text{HMoO}_x\text{-Zn}$  anodes possessed a voltage hysteresis of 220 mV without significant voltage fluctuations at an ultra-high current density of  $10.0 \text{ mA cm}^{-2}$ . The exceptional rate capability and reversibility observed in  $\text{HMoO}_x\text{-Zn}$  anodes could be attributed to the minimized dendrite formation, uniform zinc deposition/stripping, and improved corrosion resistance achieved with the  $\text{HMoO}_x$  coating. Therefore, the aforementioned results indicated that the  $\text{HMoO}_x$  coating could substantially enhance the cycling stability of zinc anodes in aqueous electrolytes.

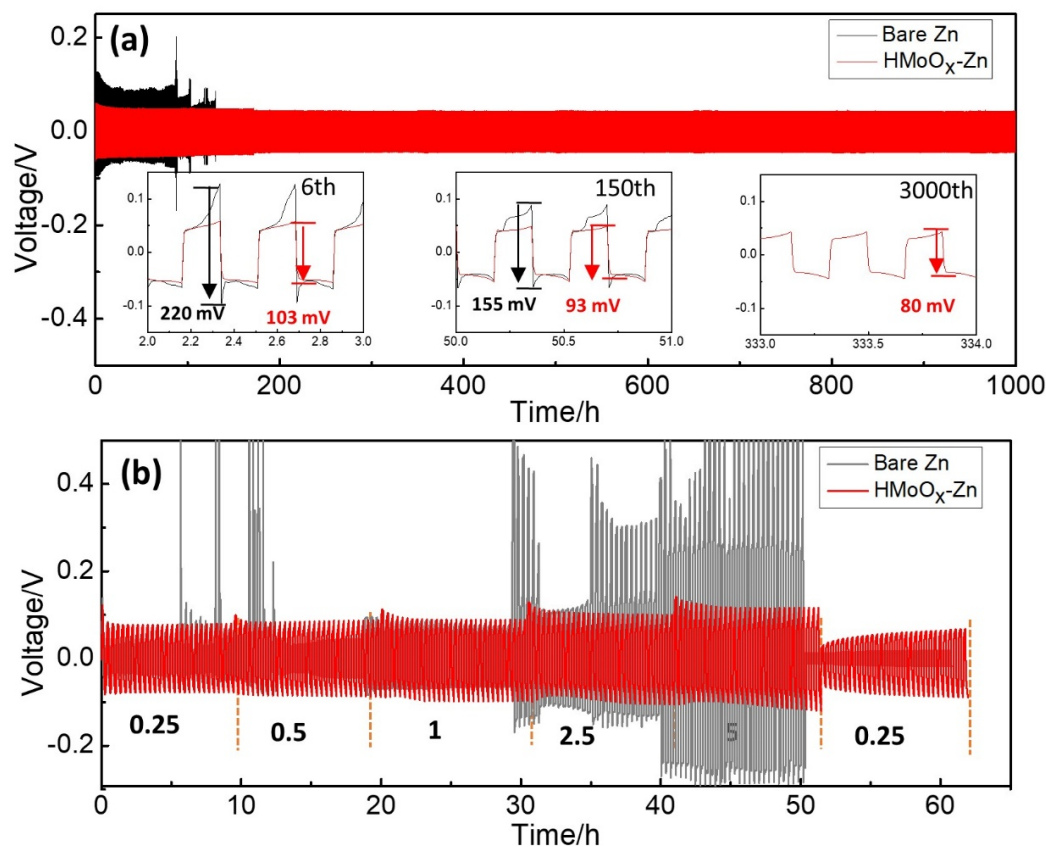


**Figure 4.** Electrochemical performance of the  $\text{HMoO}_x\text{-Zn}$  symmetrical cell. (a) The dynamic measurements of a symmetric cell for the bare Zn and  $\text{HMoO}_x\text{-Zn}$  anodes after 3000 cycles ( $2.5 \text{ mA/cm}^2$ ). (b) The symmetrical cell test for the bare Zn and  $\text{HMoO}_x\text{-Zn}$  anodes at various current densities of 0.25, 0.5, 1, 2.5, 5, and  $0.25 \text{ mA cm}^{-2}$ . The stripping/plating time of the anodes was 10 min for each cycle.

Assembled full cells were utilized to explore the effect of the  $\text{HMoO}_x$  coating on the electrochemical behavior within ZIB systems. From observing the cyclic voltammogram (CV) curves in Figure 5a,b, comparing  $\text{Zn} \parallel \gamma\text{-MnO}_2$  to  $\text{HMoO}_x\text{-Zn} \parallel \gamma\text{-MnO}_2$  full cells, the peak positions had shifted slightly. This indicated that the introduction of a  $\text{HMoO}_x$  layer can change the electrochemical properties and kinetic properties of a bare Zn electrode surface, leading to shifts in the oxidation and reduction peaks. Importantly, the  $\text{Zn} \parallel \gamma\text{-MnO}_2$  and  $\text{HMoO}_x\text{-Zn} \parallel \gamma\text{-MnO}_2$  full cells showed similar redox behavior, thus indicating the negligible influence of the  $\text{HMoO}_x$  layer on the redox reaction mechanism in the battery system. Furthermore,  $\text{HMoO}_x\text{-Zn}$  exhibited a higher peak current density, in comparison to the bare Zn, suggesting that the  $\text{HMoO}_x$  layer could promote electrochemical reactivity and capacity [48]. As exhibited in Figure 5c, the galvanostatic charge–discharge profiles of both batteries were in accordance with the CV curve analysis. In addition, the voltage difference in the  $\text{HMoO}_x\text{-Zn} \parallel \gamma\text{-MnO}_2$  full cell was obviously lower than that in the  $\text{Zn} \parallel \gamma\text{-MnO}_2$  full cell, as shown in Figure 5d. This implies a reduction in the energy required for ion extraction and insertion from the host lattice, which partly mitigated

polarization and facilitated electrochemical reactions [49]. Additionally, it underscored the role of the  $\text{HMoO}_x$  coating in regulating and protecting the Zn anode's surface, thereby boosting the overall performance of the cells.

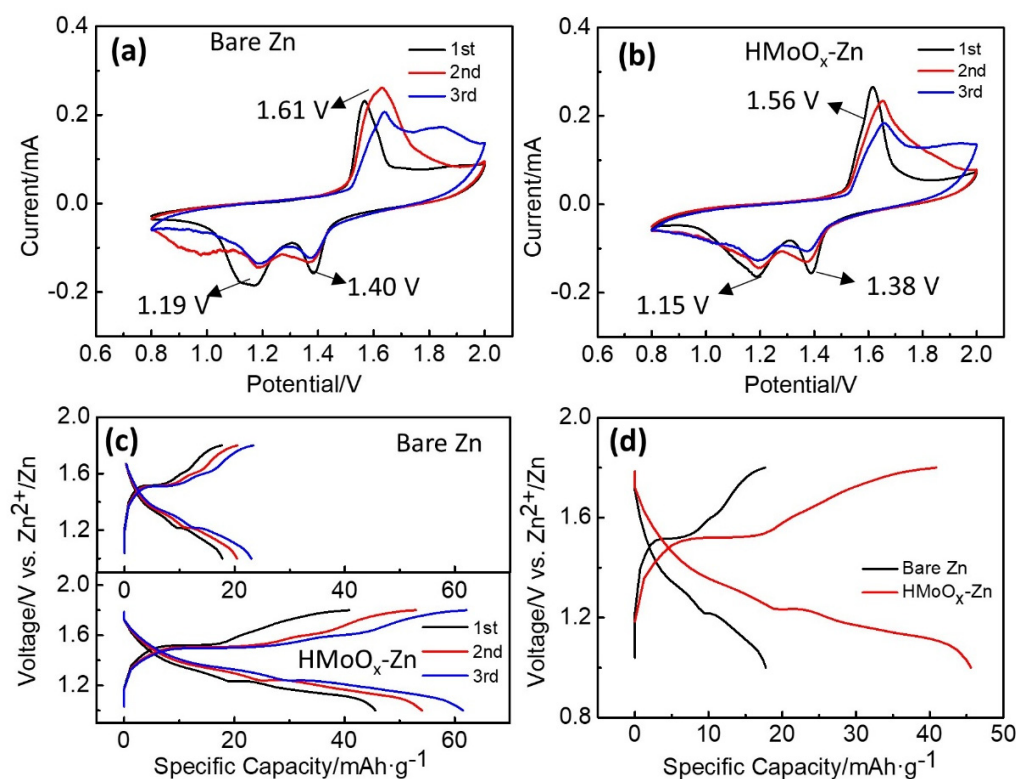


**Figure 5.** Comparison of electrochemical performance for  $\text{HMoO}_x\text{-Zn}$  (or bare Zn)  $\parallel \gamma\text{-MnO}_2$  full cells using the  $\text{ZnSO}_4$  electrolyte. (a,b) CV curves for bare Zn  $\parallel \gamma\text{-MnO}_2$  and  $\text{HMoO}_x\text{-Zn} \parallel \gamma\text{-MnO}_2$  full cells with the voltage window of 0.8–2.0 V at a sweep rate of  $0.2 \text{ mV s}^{-1}$  in the third cycle, respectively. (c) The voltage profiles for bare Zn  $\parallel \gamma\text{-MnO}_2$  full cells and  $\text{HMoO}_x\text{-Zn} \parallel \gamma\text{-MnO}_2$  between 1.0 and 1.8 V at  $0.1 \text{ A g}^{-1}$ . (d) Charge/discharge profiles of the bare Zn  $\parallel \gamma\text{-MnO}_2$  and  $\text{HMoO}_x\text{-Zn} \parallel \gamma\text{-MnO}_2$  full cells at  $0.1 \text{ A g}^{-1}$ .

Further validation of the improved cycle performance for the  $\text{HMoO}_x\text{-Zn} \parallel \gamma\text{-MnO}_2$  full cells was achieved using charge–discharge tests, with various current densities ranging from  $0.1$  to  $2.0 \text{ A g}^{-1}$ . As depicted in Figure 6a,b, the capacity of both samples rapidly diminished as the current densities increased, owing to electrochemical polarization. Nevertheless, it is noteworthy that the rate performance of the  $\text{HMoO}_x\text{-Zn} \parallel \gamma\text{-MnO}_2$  full cell exceeded that of the bare Zn  $\parallel \gamma\text{-MnO}_2$  full cell across various current densities. The specific capacity of the full cells rebounded when the current density returned to  $0.2 \text{ A g}^{-1}$ , whereas the bare Zn  $\parallel \gamma\text{-MnO}_2$  full cell exhibited a declining trend in subsequent cycling processes. Simultaneously, the cyclic stability for the bare Zn  $\parallel \gamma\text{-MnO}_2$  and  $\text{HMoO}_x\text{-Zn} \parallel \gamma\text{-MnO}_2$  full cells was tested at a relatively high current density of  $0.1 \text{ A g}^{-1}$ , as shown in Figure 6c,d. The rapid deterioration in capacity of the bare Zn  $\parallel \gamma\text{-MnO}_2$  full cell, with only  $50 \text{ mA h g}^{-1}$  remaining after 300 cycles, is illustrated in Figure 6c. Remarkably, as shown in Figure 6d, the  $\text{HMoO}_x\text{-Zn} \parallel \gamma\text{-MnO}_2$  full cell maintained a high discharge capacity of  $131 \text{ mA h g}^{-1}$  after 300 cycles at  $0.1 \text{ A g}^{-1}$ . Therefore, the  $\text{HMoO}_x$  coating could promote minimal electrode polarization and enhance cycling stability. Compared to the Zn anodes fabricated for preventing dendrite growth in the Zn anode (as reported in Table S1), the  $\text{HMoO}_x\text{-Zn}$  anode remained at a relatively high level.

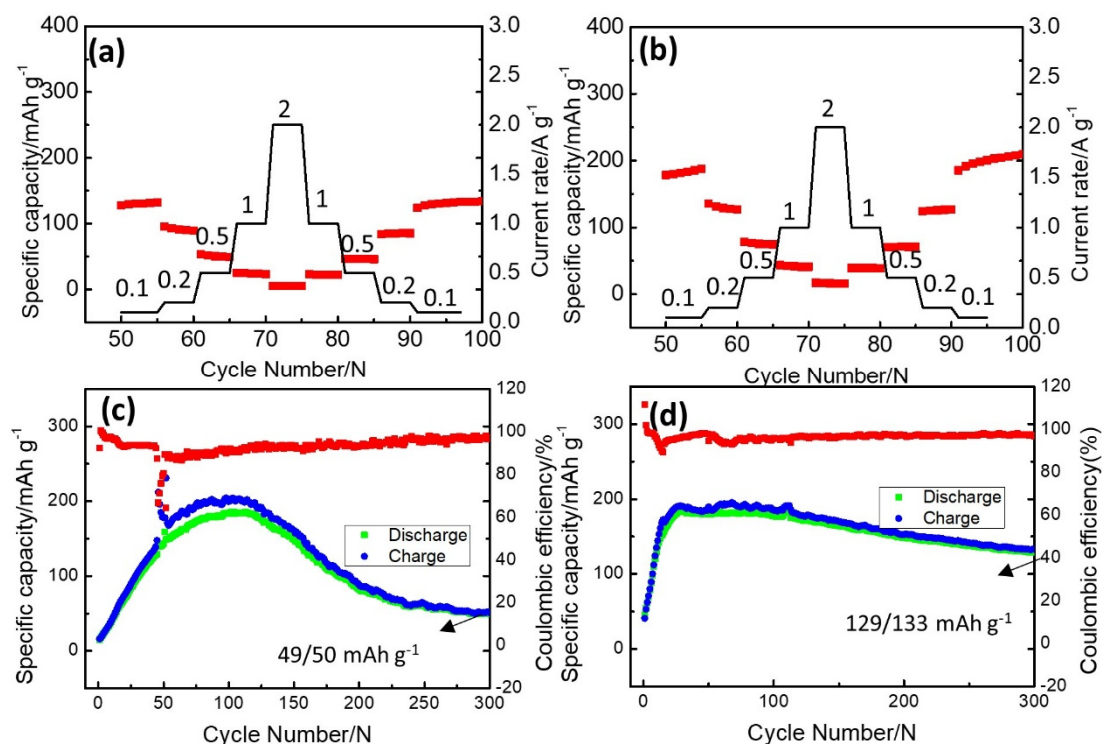


**Figure 6.** Comparison of cycle performance for HMoO<sub>x</sub>-Zn. (a,b) Rate performance at 0.1 A g<sup>-1</sup>, 0.2 A g<sup>-1</sup>, 0.5 A g<sup>-1</sup>, 1.0 A g<sup>-1</sup>, and 2.0 A g<sup>-1</sup> for the bare Zn | γ-MnO<sub>2</sub> full cell and HMoO<sub>x</sub>-Zn | γ-MnO<sub>2</sub> full cell, respectively. (c,d) Cyclic stability for the bare Zn | γ-MnO<sub>2</sub> full cell and HMoO<sub>x</sub>-Zn | γ-MnO<sub>2</sub> full cell at 0.1 A g<sup>-1</sup>, respectively (The red curve represents the corresponding coulomb efficiency).

EIS plots were measured to assess the Zn<sup>2+</sup> plating kinetics in the symmetric cells. Figure 7a depicts the EIS data of the bare Zn and HMoO<sub>x</sub>-Zn before cycle testing. Evidently, the HMoO<sub>x</sub>-Zn symmetric cells demonstrated smaller charge transfer resistance (R<sub>ct</sub>) in comparison to the bare Zn symmetric cells, suggesting that applying a HMoO<sub>x</sub> layer on the zinc could enhance the migration charge of ions, potentially alleviating the degradation of cycle performance due to polarization. This was further confirmed by the analysis results obtained from the polarization curves shown in Figure 7b. The overpotential of HMoO<sub>x</sub>-Zn was higher than that of the bare Zn, and its corrosion current was lower than that of the bare Zn, suggesting that the presence of the HMoO<sub>x</sub> layer could function as a corrosion inhibitor, guarding the zinc anode against corrosion [50]. In order to assess the corrosion resistance of zinc metal following surface coating modification, bare zinc foils and HMoO<sub>x</sub>-Zn plates were submerged in a 1 M ZnSO<sub>4</sub> aqueous electrolyte for one week. As illustrated in Figure 7c, for the Zn anode and HMoO<sub>x</sub>-Zn anode, similar diffraction peaks of new phase by-products at 16.2° and 24.6° were detected after a soaking state for a week, but the relative peak intensities of the HMoO<sub>x</sub>-Zn anode were weaker than those of the bare Zn anode. This indicated that the HMoO<sub>x</sub> layer might act as a safeguard, diminishing the rate of corrosion for zinc in the aqueous electrolyte. The SEM image in Figure 7e displayed a high number of large and irregular flaky products loosely gathered on the exposed zinc surface, indicating a significant level of chemical corrosion occurring on the surface of the zinc metal in the aqueous electrolyte. Additionally, these corrosion products could significantly hinder electron/ion diffusion, elevate interface impedance, and consequently obstruct zinc plating/stripping reactions, whereas when coated with HMoO<sub>x</sub>, only a few flakes were observed, and they were significantly smaller in size (as depicted in Figure 7d), indicating that the zinc corrosion was effectively suppressed. To investigate the impact of a HMoO<sub>x</sub> coating on Zn plates, contact angles were measured (see Figure 7f,g). The contact angles of HMoO<sub>x</sub>-Zn and bare zinc were measured at 87.69° and



100.64°, respectively. The lower contact angle of HMoO<sub>x</sub>-Zn demonstrated its superior surface wetting properties. Improving surface wettability enhanced the effective interaction between the electrolyte and the HMoO<sub>x</sub>-Zn anode while also aiding in reducing charge transfer resistance. This, in turn, promoted the migration of Zn<sup>2+</sup> ions and ensured uniform deposition [41,51]. Consequently, the prevention of zinc dendrite formation was achieved.

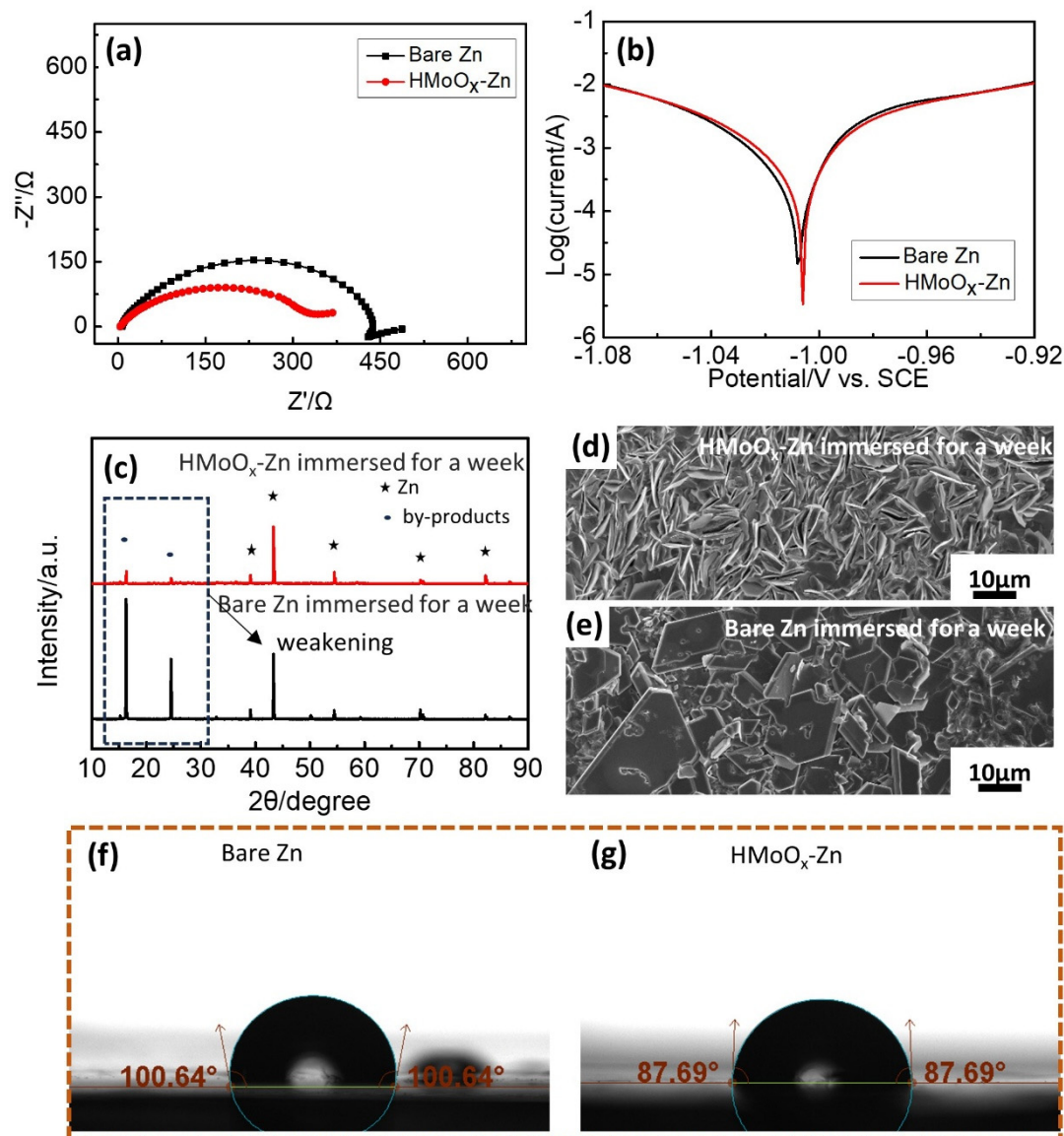


**Figure 7.** The analysis of property for the HMoO<sub>x</sub>-Zn anode. (a) The EIS spectra of bare Zn and HMoO<sub>x</sub>-Zn symmetrical batteries. (b) Polarization curves of bare Zn and HMoO<sub>x</sub>-Zn. (c) The XRD patterns and SEM of bare Zn. (d,e) The SEM of HMoO<sub>x</sub>-Zn foils after immersion in the ZnSO<sub>4</sub> aqueous electrolyte for one week. (f,g) The contact angles of the electrolyte on bare Zn and HMoO<sub>x</sub>-Zn.

The characterizations of bare Zn and HMoO<sub>x</sub>-Zn in the plating/stripping process are examined in Figure 8. SEM imaging was utilized to investigate the morphological changes in both electrodes following various states of stripping and plating, as presented in Figure 8a,b. After 50 cycles, it was obvious that the bare Zn plate exhibited an abundance of dendrites that may have developed and partially breached the separator, while the homogeneous deposition layer on the surface of HMoO<sub>x</sub>-Zn appeared to consist primarily of densely packed flake-like products. We speculated that the dense phase observed atop the HMoO<sub>x</sub> layer comprised deposited zinc metal, and the irregular flakes were

determined as sulfate by-products. The XRD patterns of the bare Zn and  $\text{HMoO}_x\text{-Zn}$  after 50 cycles are displayed in Figure 8c. It can be observed that the crystalline structures of both electrodes had no notable discrepancies, indicating that zinc plating and stripping were the predominant electrochemical reactions detected throughout the cycling process. However, several newly emerged diffraction peaks of the two electrodes corresponded to  $\text{ZnSO}_4 \cdot 3\text{Zn(OH)}_2 \cdot 4\text{H}_2\text{O}$  in Figure 8d, illustrating that side reactions, such as corrosion and hydrogen evolution, took place in both anodes during cycling [52]. Moreover, the protective layer can promote uniform Zn deposition, and this reduction in dendrite growth consequently decreased the by-products associated with dendrite formation; therefore, the peaks of Zn by-products in the modified Zn anode were lower than those in the bare Zn. Based on the preceding experimental characterization, it could be inferred that the presence of the  $\text{HMoO}_x$  layer substantially impeded dendrite growth and reduced the incidence of side reactions. In addition to its wettability, the total performance was improved. However, zinc dendrites grew vigorously on bare zinc foil without any protective measures because of the impact of the tip effect, as displayed in Figure 8e. Hence, the presence of the  $\text{HMoO}_x$  layer aided in safeguarding the zinc anode by inducing uniform deposition of  $\text{Zn}^{2+}$  and facilitating  $\text{Zn}^{2+}$  migration.

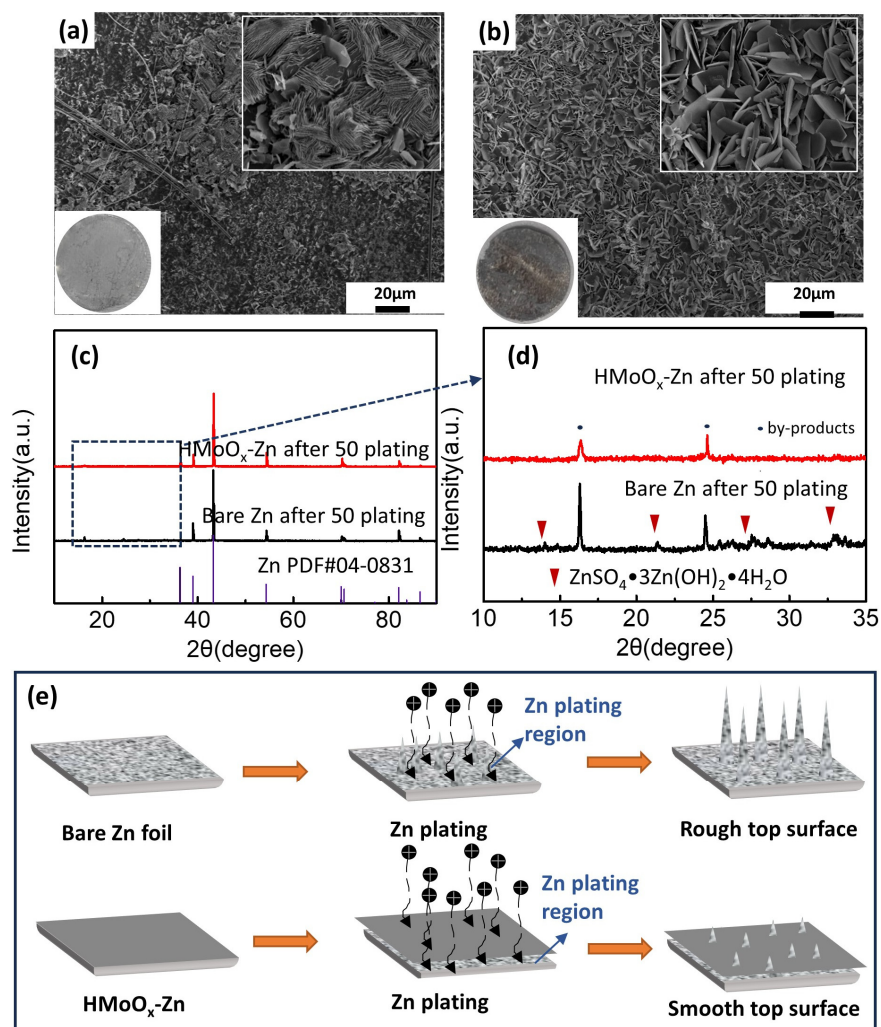


**Figure 8.** Mechanism of performance improvement for the  $\text{HMoO}_x\text{-Zn}$  anode. (a,b) The SEM images of the bare Zn and  $\text{HMoO}_x\text{-Zn}$  after 50 cycles. The insert graphs are digital photographs corresponding to Figure 8a,b. (c) The XRD patterns for bare Zn and  $\text{HMoO}_x\text{-Zn}$  after 50 plating cycles. (d) The high-resolution XRD patterns in Figure 8c are shown at low angles. (e) The schematic diagram of the dendrite inhibition mechanism of the  $\text{HMoO}_x$  coating.

In order to further illustrate the importance of the  $\text{HMoO}_x$  coating, we performed two sets of molecular dynamics simulations for the surfaces of the  $\text{HMoO}_x$ -Zn and Zn anodes. Figure 9a,b show the surface structures of both the Zn and  $\text{HMoO}_x$ -Zn anodes in the range of 0–500 ns, respectively. The presence of  $\text{HMoO}_x$  suppressed the growth of Zn dendrites by forming a protective layer by interacting with Zn ions and preventing unstable reactions in localized regions. This inhibition potentially helped maintain surface uniformity and reduced dendrite formation. Additionally,  $\text{HMoO}_x$  may have formed a barrier layer on the surface of the Zn anode, impeding the free migration of Zn ions. This barrier layer effectively slowed down the rate of dendrite expansion. The results of these simulations were consistent with the above experimental outcomes, which fully demonstrated the protective role of the  $\text{HMoO}_x$  layer on the performance of the Zn anode.

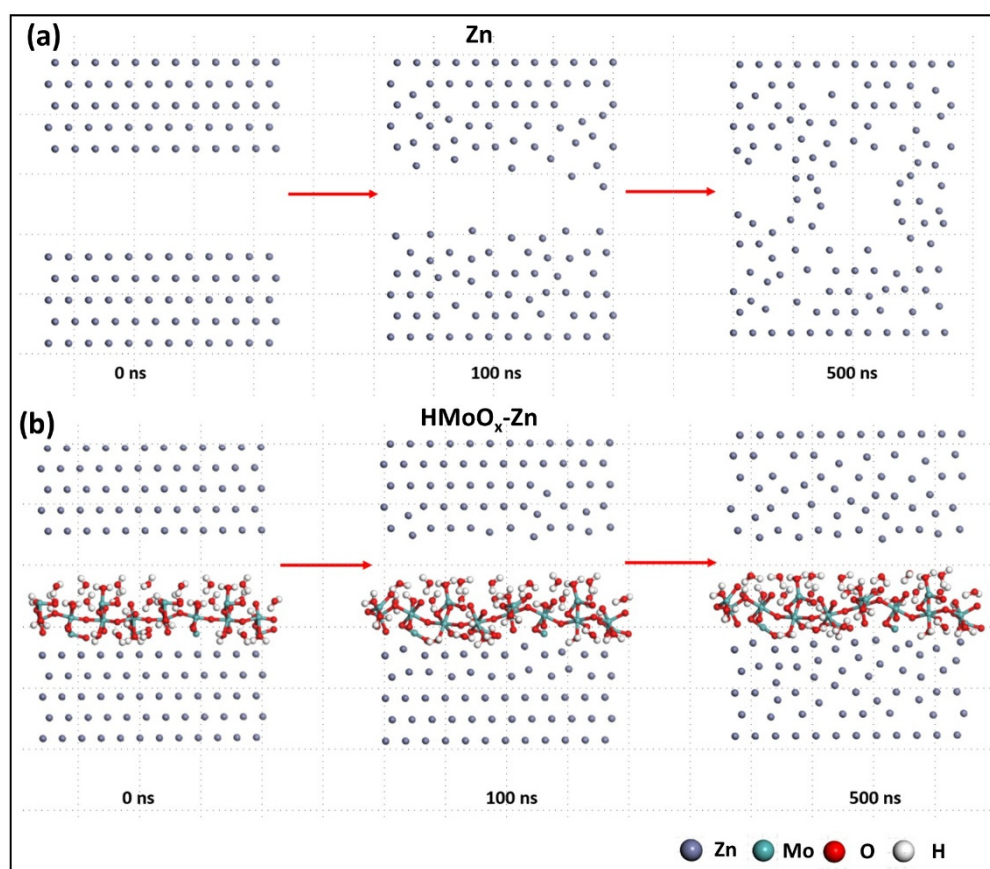


**Figure 9.** Theoretical calculation verification of the performance improvement for the  $\text{HMoO}_x$ -Zn anode. The molecular dynamics simulations for the surface of the Zn anode (a) and  $\text{HMoO}_x$ -Zn anode (b).

### 3. Materials and Methods

#### 3.1. Materials' Synthesis

For synthesizing zinc foils coated with  $\text{HMoO}_x$ , the Zn foils were purchased from Hengxing Trade Co., Ltd. (Cardiff, UK) before conducting the experiments. The surface of the bare Zn was cleaned using diluted hydrochloric acid and ethanol, respectively. The  $\text{HMoO}_x$  was electrochemically deposited onto the Zn sheet using a simple three-electrode system. The working electrode employed was a zinc sheet measuring 30  $\mu\text{m}$  in thickness and cut to dimensions of  $2.0 \times 2.5 \text{ cm}^2$ , while the deposition area was  $4 \text{ cm}^2$  to ensure the same deposition area. The reference electrode utilized was the SCE electrode, with platinum foil functioning as the counter electrode. A 5 mM solution of ammonium molybdate (Sino Pharm, Beijing, China) was utilized as the electrolyte. The space between the zinc sheet and the Pt electrode was approximately 1.5 cm. The  $\text{HMoO}_x$  layer was electrodeposited

onto the zinc foil by maintaining a potential of  $-0.8$  V for durations of 0, 20, 50, 75, 100, 150, 200, and 250 s. The Zn coated with  $\text{HMoO}_x$  underwent multiple rinses with deionized water/ethanol and was subsequently subjected to vacuum drying at  $60$  °C.

### 3.2. Materials' Characterizations

X-ray diffraction (XRD, Bruker, D8 Advances, Karlsruhe, Germany) was employed to study the crystallographic phase of the samples. Scanning electron microscopy (SEM; Regulus 8100, Hitachi, Japan) was carried out to study the morphology of the samples. The contact angles of electrolyte droplets (1 M  $\text{ZnSO}_4$ ) on the bare zinc and  $\text{HMoO}_x$ -coated zinc were measured using the Dataphysics DCAT21 instrument. X-ray photoelectron spectroscopy (XPS; Shimadzu AXIS ULTRA DLD, Kyoto, Japan) was utilized to determine the chemical or electronic configurations of elements

### 3.3. Electrochemical Measurements

To evaluate the plating/stripping behaviors and cyclic durability of the bare Zn and  $\text{HMoO}_x$ -Zn anodes in charge and discharge processes, symmetric cell setups were created by pairing identical  $\text{HMoO}_x$ -Zn anodes (or bare Zn foils) measuring 16 mm in diameter. The glass fiber was employed as a separator (Whatman, Grade GF/A, English) and  $\text{ZnSO}_4$  aqueous solution (1 M) was used as the electrolyte. The long-term cycle and rate performance of symmetrical batteries were tested under different current densities utilizing the NEWARE battery testing instrument. The corrosion behavior was assessed via linear polarization, employing  $\text{HMoO}_x$ -Zn (or bare Zn) for both the counter and working electrodes, and utilizing SCE as the reference electrode in a 1 M  $\text{ZnSO}_4$  solution, with a scan rate set at  $5$  mV  $\text{s}^{-1}$ .

To assess the electrochemical performance of  $\text{HMoO}_x$ -Zn/ $\gamma$ - $\text{MnO}_2$  (bare Zn/ $\gamma$ - $\text{MnO}_2$ ) full batteries, a slurry was prepared by mixing the active materials  $\gamma$ - $\text{MnO}_2$  (Chizhou Jingyan New Energy Technology Co., Ltd., Chizhou, Anhui province, China > 99.0%), acetylene black, and polyvinyl difluoride in a weight ratio of 8:1:1, along with a suitable quantity of N-methyl pyrrolidone solvent. The mixture was subsequently spread onto a titanium foil and dried under vacuum conditions at  $90$  °C for a period of 18 h. Circular electrodes with a diameter of 12 mm were cut from the sheets, achieving a calculated mass loading of approximately  $0.93$  mg  $\text{cm}^{-2}$  for  $\gamma$ - $\text{MnO}_2$ . The full cells were assembled into CR2025 coin cells under ambient atmospheric conditions, featuring  $\text{HMoO}_x$ -Zn (or bare Zn) foil anodes and  $\gamma$ - $\text{MnO}_2$  cathodes, separated by a 19 mm-diameter glass fiber separator, and utilizing a 1 M  $\text{ZnSO}_4$  aqueous solution as the electrolyte. Galvanostatic charge/discharge processes were performed by the NEWARE battery testing instrument within the voltage range of 1.0–1.8 V (vs.  $\text{Zn}^{2+}/\text{Zn}$ ). The electrochemical workstation (CHI660E, Shanghai Chenhua Instrument Co., Ltd, Shanghai, China) was utilized for conducting electrochemical impedance spectroscopy (EIS) and cyclic voltammetry (CV). All test conditions were controlled at  $25$  °C unless otherwise specified.

### 3.4. Theoretical Calculations

The VASP code was used to perform density functional theory (DFT) calculations [53]. Under generalized gradient approximation (GGA), the Perdew–Burke–Ernzerhof (PBE) functional was employed to compute the exchange correlation [54]. In order to describe the expansion of the electronic eigenfunctions, a projector-augmented wave (PAW) pseudopotential, configured with a kinetic energy cut-off of 500 eV, was utilized [55]. The vacuum thickness was adjusted to 15 Å in order to minimize interlayer interactions. The  $\Gamma$ -centered  $5 \times 5 \times 1$  Monkhorst–Pack k points were utilized for sampling the Brillouin-zone integration, and all atomic positions underwent complete relaxation until energy and force, respectively, reached a tolerance of  $1 \times 10^{-5}$  eV and  $0.03$  eV/Å. The long-range interactions were illustrated by the dispersion-corrected DFT–D method [56].



#### 4. Conclusions

In summary, a HMoO<sub>x</sub> coating was synthesized on the zinc surface via a straightforward electrodeposition method, employed as the anode material for aqueous ZIBs. The HMoO<sub>x</sub> coating effectively mitigated corrosion and suppressed side reactions during Zn deposition/stripping. It also improved surface wettability and reduced the interfacial impedance, which was beneficial to facilitate Zn<sup>2+</sup> migration and uniform deposition of Zn<sup>2+</sup>, thereby inhibiting dendrite formation on the zinc anode. The symmetric cell with the HMoO<sub>x</sub>-coated zinc anode demonstrated remarkable long-term cycle stability, maintaining an exceptionally low-voltage hysteresis of 80 mV at 2.5 mA cm<sup>-2</sup> over 3000 cycles. Additionally, the HMoO<sub>x</sub>-Zn || γ-MnO<sub>2</sub> full cell exhibited a notably enhanced cycle and rate performance, achieving a high discharge capacity of 131 mAh g<sup>-1</sup> after 300 cycles at 0.1 A g<sup>-1</sup>. Moreover, the simulation of the HMoO<sub>x</sub>-Zn anode verified the protective role of the HMoO<sub>x</sub> layer on the performance of the zinc anode. This research offers an innovative approach for designing dendrite-free zinc anodes in high-performance, metal-based batteries and can also be extended to the protection of other metal anodes.

**Supplementary Materials:** The following supporting information can be downloaded at: <https://www.mdpi.com/article/10.3390/molecules29133229/s1>, Figure S1: Galvanostatic cycling performances of bare Zn symmetrical cells with at different deposition times of 20 s, 50 s, 75s, 100 s, 150 s, 200 s at a current density of 2.5 mA cm<sup>-2</sup>; Figure S2: (a,b) The SEM of HMoO<sub>x</sub>-Zn anode at different deposition times of 20 s and 100 s; Figure S3: The TEM of HMoO<sub>x</sub> at various magnification. Table S1: Comparison reported Zn anodes fabricated for preventing dendrite growth.

**Author Contributions:** J.Y., X.C. and H.S.: methodology, investigation, data curation, funding acquisition, and writing—original draft; W.B. and W.Z.: resources, funding acquisition; Y.S., H.W., Y.C. and C.Z.: methodology, validation, and writing—review. All authors have read and agreed to the published version of the manuscript.

**Funding:** Financial support for this study was received from the National Natural Science Foundation of China (No. 22102012, No. 22272011, No. 22309018, and No. 22202022), the Changzhou Science and Technology Plan Applied Basic Research Project (CJ20230039, CJ20235068, and CJ20235070), the Natural Science Foundation of the Jiangsu Higher Education Institutions of China (22KJB530005 and 23KJB480003), and the research fund of Jiangsu Province Engineering Research Center of Intelligent Manufacturing Technology for the New Energy Vehicle Power Battery.

**Institutional Review Board Statement:** Not applicable.

**Informed Consent Statement:** Not applicable.

**Data Availability Statement:** Data are contained within the article and Supplementary Materials.

**Conflicts of Interest:** We have no financial and personal relationships with other people or organizations that can inappropriately influence our work.

#### References

1. Lin, Z.; Fan, K.; Liu, T.; Xu, Z.; Chen, G.; Zhang, H.; Li, H.; Guo, X.; Zhang, X.; Zhu, Y. Mitigating lattice distortion of high-voltage LiCoO<sub>2</sub> via core-shell structure induced by cationic heterogeneous Co-Doping for lithium-ion batteries. *Nano-Micro Lett.* **2024**, *16*, 48. [CrossRef] [PubMed]
2. Chen, X.; Liu, T.; Ding, Y.; Sun, X.; Huang, J.; Qiao, J.; Peng, S. Controlled nucleation and growth for the dendrite-free zinc anode in aqueous zinc-ion battery. *J. Alloys Compd.* **2024**, *970*, 172584. [CrossRef]
3. Zhang, Y.; Li, D.; Li, J.; Li, Y.; Wang, L.; Xu, H.; Han, W. Flexible TiVCT<sub>x</sub> MXene film for high-performance magnesium-ion storage device. *J. Colloid Interface Sci.* **2024**, *657*, 550–558. [CrossRef]
4. Mathiyalagan, K.; Shin, D.; Lee, Y.-C. Difficulties, strategies, and recent research and development of layered sodium transition metal oxide cathode materials for high-energy sodium-ion batteries. *J. Energy Chem.* **2023**, *90*, 40–57. [CrossRef]
5. Wang, Y.; Gu, H.; Lu, Y.; Zhang, W.; Li, Z. The synergistic effect of Lewis acidic etching V<sub>4</sub>C<sub>3</sub> (MXene)@ CuSe<sub>2</sub>/CoSe<sub>2</sub> as an advanced cathode material for aluminum batteries. *J. Mater. Sci. Technol.* **2024**, *177*, 205–213. [CrossRef]
6. Gu, H.; Yang, X.; Chen, S.; Zhang, W.; Yang, H.Y.; Li, Z. Oxygen vacancies boosted proton intercalation kinetics for aqueous aluminum-manganese Batteries. *Nano Lett.* **2023**, *23*, 11842–11849. [CrossRef] [PubMed]
7. Gonçalves, J.M.; Santos, É.A.; Martins, P.R.; Silva, C.G.; Zanin, H. Emerging medium- and high-entropy materials as catalysts for lithium-sulfur batteries. *Energy Storage Mater.* **2023**, *63*, 102999. [CrossRef]

8. Li, X.; Ye, P.; Dou, A.; Jiang, Z.; Naveed, A.; Zhou, Y.; Su, M.; Zhang, P.; Liu, Y. Nanoporous Nb<sub>2</sub>O<sub>5</sub> coatings enabled long-life and deeply rechargeable zinc anodes for aqueous zinc-ion batteries. *J. Energy Storage* **2024**, *76*, 109874. [[CrossRef](#)]
9. Li, L.; Zhang, Y.; Du, C.; Zhou, X.; Xiong, H.; Wang, G.; Lu, X. Achieving stable Zn metal anode via a hydrophobic and Zn<sup>2+</sup>-conductive amorphous carbon interface. *J. Colloid Interface Sci.* **2024**, *657*, 644–652. [[CrossRef](#)]
10. Zhao, J.; Ying, Y.; Wang, G.; Hu, K.; Di Yuan, Y.; Ye, H.; Liu, Z.; Lee, J.Y.; Zhao, D. Covalent organic framework film protected zinc anode for highly stable rechargeable aqueous zinc-ion batteries. *Energy Storage Mater.* **2022**, *48*, 82–89. [[CrossRef](#)]
11. Zhang, Y.; Yang, X.; Hu, Y.; Hu, K.; Lin, X.; Liu, X.; Reddy, K.M.; Xie, G.; Qiu, H.J. Highly strengthened and toughened Zn–Li–Mn alloys as long-cycling life and dendrite-free Zn anode for aqueous zinc-ion batteries. *Small* **2022**, *18*, 2200787. [[CrossRef](#)] [[PubMed](#)]
12. Liu, M.; Hu, A.; Yan, Z.; Chen, J.; He, M.; Zhou, B.; Pan, Y.; Fan, Y.; Gao, D.; Long, J. Enhancing Zn<sup>2+</sup> diffusion for dendrite-free zinc anodes via a robust zincophilic clay mineral coating. *Chem. Eng. J.* **2024**, *479*, 147410. [[CrossRef](#)]
13. Xu, P.; Wang, C.; Zhao, B.; Zhou, Y.; Cheng, H. An interfacial coating with high corrosion resistance based on halloysite nanotubes for anode protection of zinc-ion batteries. *J. Colloid Interface Sci.* **2021**, *602*, 859–867. [[CrossRef](#)] [[PubMed](#)]
14. Yang, Z.; Hu, C.; Zhang, Q.; Wu, T.; Xie, C.; Wang, H.; Tang, Y.; Ji, X.; Wang, H. Bulk-phase reconstruction enables robust Zinc metal anodes for aqueous Zinc-Ion batteries. *Angew. Chem.* **2023**, *135*, e202308017. [[CrossRef](#)]
15. Wang, S.-B.; Ran, Q.; Yao, R.-Q.; Shi, H.; Wen, Z.; Zhao, M.; Lang, X.-Y.; Jiang, Q. Lamella-nanostructured eutectic zinc-aluminum alloys as reversible and dendrite-free anodes for aqueous rechargeable batteries. *Nat. Commun.* **2020**, *11*, 1634. [[CrossRef](#)]
16. Zhu, C.; Li, P.; Xu, G.; Cheng, H.; Gao, G. Recent progress and challenges of Zn anode modification materials in aqueous Zn-ion batteries. *Coord. Chem. Rev.* **2023**, *485*, 215142. [[CrossRef](#)]
17. Zhou, J.; Xie, M.; Wu, F.; Mei, Y.; Hao, Y.; Li, L.; Chen, R. Encapsulation of metallic Zn in a hybrid MXene/Graphene aerogel as a stable Zn anode for foldable Zn-Ion batteries. *Adv. Mater.* **2022**, *34*, 2106897. [[CrossRef](#)] [[PubMed](#)]
18. Su, Y.; Wang, X.; Zhou, S.; Zou, X.; Sun, H.; Liu, D.; Zhu, G. A specific free-volume network as synergistic zinc-ion-conductor interface towards stable zinc anode. *Energy Storage Mater.* **2022**, *53*, 909–916. [[CrossRef](#)]
19. Kang, L.; Cui, M.; Jiang, F.; Gao, Y.; Luo, H.; Liu, J.; Liang, W.; Zhi, C. Nanoporous CaCO<sub>3</sub> coatings enabled uniform Zn stripping/plating for long-life zinc rechargeable aqueous batteries. *Adv. Energy Mater.* **2018**, *8*, 1801090. [[CrossRef](#)]
20. Tao, F.; Liu, Y.; Ren, X.; Wang, J.; Zhou, Y.; Miao, Y.; Ren, F.; Wei, S.; Ma, J. Different surface modification methods and coating materials of zinc metal anode. *J. Energy Chem.* **2022**, *66*, 397–412. [[CrossRef](#)]
21. Naveed, A.; Yang, H.; Yang, J.; Nuli, Y.; Wang, J. Highly reversible and rechargeable safe Zn batteries based on a triethyl phosphate electrolyte. *Angew. Chem. Int. Ed.* **2019**, *58*, 2760–2764. [[CrossRef](#)] [[PubMed](#)]
22. Naveed, A.; Yang, H.; Shao, Y.; Yang, J.; Yanna, N.; Liu, J.; Shi, S.; Zhang, L.; Ye, A.; He, B. A highly reversible Zn anode with intrinsically safe organic electrolyte for long-cycle-life batteries. *Adv. Mater.* **2019**, *31*, 1900668. [[CrossRef](#)] [[PubMed](#)]
23. Zhong, Y.; Cheng, Z.; Zhang, H.; Li, J.; Liu, D.; Liao, Y.; Meng, J.; Shen, Y.; Huang, Y. Monosodium glutamate, an effective electrolyte additive to enhance cycling performance of Zn anode in aqueous battery. *Nano Energy* **2022**, *98*, 107220. [[CrossRef](#)]
24. Shen, F.; Du, H.; Qin, H.; Wei, Z.; Kuang, W.; Hu, N.; Lv, W.; Yi, Z.; Huang, D.; Chen, Z. Mediating triple ions migration behavior via a fluorinated separator interface toward highly reversible aqueous Zn batteries. *Small* **2024**, *20*, 2305119. [[CrossRef](#)] [[PubMed](#)]
25. Shen, C.; Li, X.; Li, N.; Xie, K.; Wang, J.-G.; Liu, X.; Wei, B. Graphene-boosted, high-performance aqueous Zn-ion battery. *ACS Appl. Mater. Interfaces* **2018**, *10*, 25446–25453. [[CrossRef](#)] [[PubMed](#)]
26. Wang, A.; Zhou, W.; Huang, A.; Chen, M.; Chen, J.; Tian, Q.; Xu, J. Modifying the Zn anode with carbon black coating and nanofibrillated cellulose binder: A strategy to realize dendrite-free Zn–MnO<sub>2</sub> batteries. *J. Colloid Interface Sci.* **2020**, *577*, 256–264. [[CrossRef](#)] [[PubMed](#)]
27. Li, M.; He, Q.; Li, Z.; Li, Q.; Zhang, Y.; Meng, J.; Liu, X.; Li, S.; Wu, B.; Chen, L. A novel dendrite-free Mn<sup>2+</sup>/Zn<sup>2+</sup> hybrid battery with 2.3 V voltage window and 11000-cycle lifespan. *Adv. Energy Mater.* **2019**, *9*, 1901469. [[CrossRef](#)]
28. Hao, J.; Li, B.; Li, X.; Zeng, X.; Zhang, S.; Yang, F.; Liu, S.; Li, D.; Wu, C.; Guo, Z. An in-depth study of Zn metal surface chemistry for advanced aqueous Zn-ion batteries. *Adv. Mater.* **2020**, *32*, 2003021. [[CrossRef](#)]
29. He, H.; Tong, H.; Song, X.; Song, X.; Liu, J. Highly stable Zn metal anodes enabled by atomic layer deposited Al<sub>2</sub>O<sub>3</sub> coating for aqueous zinc-ion batteries. *J. Mater. Chem. A* **2020**, *8*, 7836–7846. [[CrossRef](#)]
30. Liang, P.; Yi, J.; Liu, X.; Wu, K.; Wang, Z.; Cui, J.; Liu, Y.; Wang, Y.; Xia, Y.; Zhang, J. Highly reversible Zn anode enabled by controllable formation of nucleation sites for Zn-based batteries. *Adv. Funct. Mater.* **2020**, *30*, 1908528. [[CrossRef](#)]
31. Hieu, L.T.; So, S.; Kim, I.T.; Hur, J. Zn anode with flexible β-PVDF coating for aqueous Zn-ion batteries with long cycle life. *Chem. Eng. J.* **2021**, *411*, 128584. [[CrossRef](#)]
32. Zhao, Z.; Zhao, J.; Hu, Z.; Li, J.; Li, J.; Zhang, Y.; Wang, C.; Cui, G. Long-life and deeply rechargeable aqueous Zn anodes enabled by a multifunctional brightener-inspired interphase. *Energy Environ. Sci.* **2019**, *12*, 1938–1949. [[CrossRef](#)]
33. Zhang, F.; Wang, C.; Pan, J.; Tian, F.; Zeng, S.; Yang, J.; Qian, Y. Polypyrrole-controlled plating/stripping for advanced zinc metal anodes. *Mater. Today Energy* **2020**, *17*, 100443. [[CrossRef](#)]
34. Pu, X.; Jiang, B.; Wang, X.; Liu, W.; Dong, L.; Kang, F.; Xu, C. High-performance aqueous zinc-ion batteries realized by MOF materials. *Nano-Micro Lett.* **2020**, *12*, 152. [[CrossRef](#)] [[PubMed](#)]
35. Yang, H.; Chang, Z.; Qiao, Y.; Deng, H.; Mu, X.; He, P.; Zhou, H. Constructing a super-saturated electrolyte front surface for stable rechargeable aqueous zinc batteries. *Angew. Chem.* **2020**, *132*, 9463–9467. [[CrossRef](#)]

36. Liu, M.; Yang, L.; Liu, H.; Amine, A.; Zhao, Q.; Song, Y.; Yang, J.; Wang, K.; Pan, F. Artificial solid–electrolyte interface facilitating dendrite–free zinc metal anodes via nanowetting effect. *ACS Appl. Mater. Interfaces* **2019**, *11*, 32046–32051. [[CrossRef](#)]
37. Jin, S.; Chen, Z.; Bai, S.; Zhang, Y. Highly reversible Zn anode enabled by porous BaSO<sub>4</sub> coating with wide band gap and high dielectric constant. *J. Power Sources* **2024**, *591*, 233894. [[CrossRef](#)]
38. Lin, Y.; Ta, L.; Meng, J.; Song, Y.; Liu, X.-X. Electrodepositing amorphous molybdenum oxides for aqueous NH<sup>4+</sup> storage. *Chem. Commun.* **2023**, *59*, 1481–1484. [[CrossRef](#)] [[PubMed](#)]
39. Gao, Q.; Yang, L.; Lu, X.; Mao, J.; Zhang, Y.; Wu, Y.; Tang, Y. Synthesis, characterization and lithium–storage performance of MoO<sub>2</sub>/carbon hybrid nanowires. *J. Mater. Chem.* **2010**, *20*, 2807–2812. [[CrossRef](#)]
40. Shi, J.; Hou, Y.; Liu, Z.; Zheng, Y.; Wen, L.; Su, J.; Li, L.; Liu, N.; Zhang, Z.; Gao, Y. The high–performance MoO<sub>3–x</sub>/MXene cathodes for zinc–ion batteries based on oxygen vacancies and electrolyte engineering. *Nano Energy* **2022**, *91*, 106651. [[CrossRef](#)]
41. Li, B.; Xue, J.; Lv, X.; Zhang, R.; Ma, K.; Wu, X.; Dai, L.; Wang, L.; He, Z. A facile coating strategy for high stability aqueous zinc ion batteries: Porous rutile nano–TiO<sub>2</sub> coating on zinc anode. *Surf. Coat. Technol.* **2021**, *421*, 127367. [[CrossRef](#)]
42. Noori, Y.J.; Thomas, S.; Ramadan, S.; Smith, D.E.; Greenacre, V.K.; Abdelazim, N.; Han, Y.; Beanland, R.; Hector, A.L.; Klein, N.; et al. Large–area electrodeposition of few–Layer MoS<sub>2</sub> on graphene for 2D material heterostructures. *ACS Appl. Mater. Interfaces* **2020**, *12*, 49786–49794. [[CrossRef](#)]
43. Bhoyate, S.; Mhin, S.; Jeon, J.-e.; Park, K.; Kim, J.; Choi, W. Stable and high–energy–density Zn–ion rechargeable batteries based on a MoS<sub>2</sub>–coated Zn anode. *ACS Appl. Mater. Interfaces* **2020**, *12*, 27249–27257. [[CrossRef](#)]
44. Cao, H.-Z.; Tong, C.-J.; Zhang, H.-B.; Zheng, G.-Q. Mechanism of MoO<sub>2</sub> electrodeposition from ammonium molybdate solution. *Trans. Nonferrous Met. Soc. China* **2019**, *29*, 1744–1752. [[CrossRef](#)]
45. Ravichandran, K.; Dineshbabu, N.; Arun, T.; Manivasaham, A.; Sindhuja, E. Synergistic effects of Mo and F doping on the quality factor of ZnO thin films prepared by a fully automated home–made nebulizer spray technique. *Appl. Surf. Sci.* **2017**, *392*, 624–633. [[CrossRef](#)]
46. Li, Y.; Guan, Q.; Cheng, J.; Wang, B. Amorphous H<sub>0.82</sub>MoO<sub>3.26</sub> cathodes based long cycle life fiber–shaped Zn–ion battery for wearable sensors. *Energy Storage Mater.* **2022**, *49*, 227–235. [[CrossRef](#)]
47. Zhang, Y.; Ouyang, B.; Xu, J.; Jia, G.; Chen, S.; Rawat, R.S.; Fan, H.J. Rapid synthesis of cobalt nitride nanowires: Highly efficient and low-cost catalysts for oxygen evolution. *Angew. Chem.* **2016**, *128*, 8812–8816. [[CrossRef](#)]
48. Cao, K.; Liu, H.; Li, Y.; Wang, Y.; Jiao, L. Encapsulating sulfur in δ–MnO<sub>2</sub> at room temperature for Li–S battery cathode. *Energy Storage Mater.* **2017**, *9*, 78–84. [[CrossRef](#)]
49. Wang, M.; Cao, C.; Su, F.; Wang, Y.; Liu, L.; Wang, W.; Zhang, W.; Shen, H.; Zhang, J. Optimized cyclic durability of α–MnO<sub>2</sub> nanosheets for zinc ion storage through synergistic effect of lithium ions pre–embedding and electrolyte additives. *Electrochim. Acta* **2022**, *403*, 139699. [[CrossRef](#)]
50. Ye, P.; Li, X.; He, K.; Dou, A.; Wang, X.; Naveed, A.; Zhou, Y.; Su, M.; Zhang, P.; Liu, Y. A semi–interpenetrating network polymer coating for dendrite–free Zn anodes. *J. Power Sources* **2023**, *558*, 232622. [[CrossRef](#)]
51. Zhao, K.; Wang, C.; Yu, Y.; Yan, M.; Wei, Q.; He, P.; Dong, Y.; Zhang, Z.; Wang, X.; Mai, L. Ultrathin surface coating enables stabilized zinc metal anode. *Adv. Mater. Interfaces* **2018**, *5*, 1800848. [[CrossRef](#)]
52. Cao, J.; Zhang, D.; Gu, C.; Zhang, X.; Okhawilai, M.; Wang, S.; Han, J.; Qin, J.; Huang, Y. Modulating Zn deposition via ceramic–cellulose separator with interfacial polarization effect for durable zinc anode. *Nano Energy* **2021**, *89*, 106322. [[CrossRef](#)]
53. Kresse, G.; Furthmüller, J. Efficiency of ab–initio total energy calculations for metals and semiconductors using a plane–wave basis set. *Comput. Mater. Sci.* **1996**, *6*, 15–50. [[CrossRef](#)]
54. Perdew, J.P.; Burke, K.; Ernzerhof, M. Generalized gradient approximation made simple. *Phys. Rev. Lett.* **1996**, *77*, 3865. [[CrossRef](#)]
55. Blöchl, P.E. Projector augmented–wave method. *Phys. Rev. B* **1994**, *50*, 17953. [[CrossRef](#)] [[PubMed](#)]
56. Grimme, S. Semiempirical GGA–type density functional constructed with a long–range dispersion correction. *J. Comput. Chem.* **2006**, *27*, 1787–1799. [[CrossRef](#)]

**Disclaimer/Publisher’s Note:** The statements, opinions and data contained in all publications are solely those of the individual author(s) and contributor(s) and not of MDPI and/or the editor(s). MDPI and/or the editor(s) disclaim responsibility for any injury to people or property resulting from any ideas, methods, instructions or products referred to in the content.